Journal of Materials Chemistry B

ROYAL SOCIETY OF CHEMISTRY

PAPER

View Article Online
View Journal | View Issue

Check for updates

Cite this: J. Mater. Chem. B, 2021, 9, 7271

Carambola-like Bi_2Te_3 superstructures with enhanced photoabsorption for highly efficient photothermal therapy in the second near-infrared biowindow†

Ying Zhao,[ab] Yang Liu,[ab] Qishun Wang,[c] Jianhua Liu,[d] Songtao Zhang,[a] Tianqi Zhang,[d] Daguang Wang,[e] Yinghui Wang,*[a] Longhai Jin*[d] and Hongjie Zhang*[abc]

Received 30th March 2021,
Accepted 24th May 2021

DOI: 10.1039/d1tb00694k

rsc.li/materials-b

Photothermal therapy (PTT) stimulated by light in the second near-infrared (NIR-II) biowindow shows great superiorities in the penetration ability of tissue and maximum permissible exposure (MPE). Exploring new photothermal agents with good optical absorbance in the NIR-II region is highly desirable for efficient cancer therapy. Herein, we successfully prepare carambola-like bismuth telluride (Bi_2Te_3) superstructures modified with PEGylated phospholipid (Bi_2Te_3@PEG) for CT imaging-guided PTT in the NIR-II biowindow. Attributing to their superstructures, Bi_2Te_3@PEG exhibited enhanced photoabsorption with higher photothermal conversion efficiency (55.3% for 1064 nm) compared with that of Bi_2Te_3 nanoparticles. Furthermore, the good X-ray attenuation capacity of Bi endows Bi_2Te_3@PEG with an outstanding performance as computed tomography (CT) contrast agents. Bi_2Te_3@PEG superstructures have been confirmed to effectively eliminate tumor *in vitro* and *in vivo* with negligible long-term toxicities, offering them great potential to act as theranostic platforms for cancer diagnosis and treatment.

Published on 25 Mai 2021. Downloaded on 30/01/2026 18:03:13.

Introduction

Nanomaterials integrated with imaging and treatment into one system have attracted ever-increasing attention in recent years since they are regarded as promising tools for cancer theranostics.[1] Compared with traditional cancer treatments, for instance chemotherapy, radiotherapy, and surgery,[2] photothermal therapy (PTT) is a promising alternative strategy due to its fascinating advantages, including minimal invasiveness, high spatial controllability and being less harmful to normal tissues.[3,4] Most of the nanomaterials with good absorbance in the near-infrared (NIR) region have been explored due to their potential applications in PTT, including noble metal materials,[5–7] carbon-based nanomaterials,[8–10] metal chalcogenide nanomaterials,[11,12] and so on. However, the majority of photothermal agents (PTAs) are triggered by light in the first NIR biowindow (NIR-I, 750–1000 nm) for PTT, which dramatically limits their use in clinical applications due to their low maximum permissible exposure (MPE, 0.33 W cm^{-2} for 808 nm).[13,14] By contrast, light in the NIR-II biowindow (1000–1350 nm), with higher MPE (for example, 1.0 W cm^{-2} for 1064 nm), deeper tissue penetration ability, and lower light scattering, is more suitable for PTT.[15,16] However, PTAs triggered by light in the NIR-II biowindow for PTT have rarely been reported until recently as a result of their absorption limitations in the NIR-II biowindow.[17] Therefore, it is urgent to design novel PTAs with strong absorption in the NIR-II biowindow and high photothermal conversion efficiencies (PCE, η).

To achieve imaging-guided therapy, PTAs are usually combined with nanostructures with imaging functions, for instance, magnetic resonance imaging (MRI),[18,19] photoacoustic imaging (PAI),[20] X-ray computed tomography (CT)[21–23] and so on, which can not only diagnose the tumor location, but also show the accumulation ability of PTAs in the tumor site.[24] Among them, CT is a powerful and widely used diagnostic technology with infinite tissue penetration, high spatial resolution and three-dimensional (3D) visualization of the full body.[25] Bismuth-based nanomaterials

[a] State Key Laboratory of Rare Earth Resource Utilization, Changchun Institute of Applied Chemistry (CIAC), Chinese Academy of Sciences, Changchun 130022, China. E-mail: yhwang@ciac.ac.cn, hongjie@ciac.ac.cn
[b] University of Science and Technology of China, Hefei 230026, China
[c] Department of Chemistry, Tsinghua University, Beijing 100084, China
[d] The second hospital of Jilin University, Changchun 130041, China. E-mail: jinlonghai@jlu.edu.cn
[e] Department of Gastric and Colorectal Surgery, the First Hospital, Jilin University, Changchun 130021, China

† Electronic supplementary information (ESI) available. See DOI: 10.1039/d1tb00694k

Published on 25 Mai 2021. Downloaded on 30/01/2026 18:03:13.

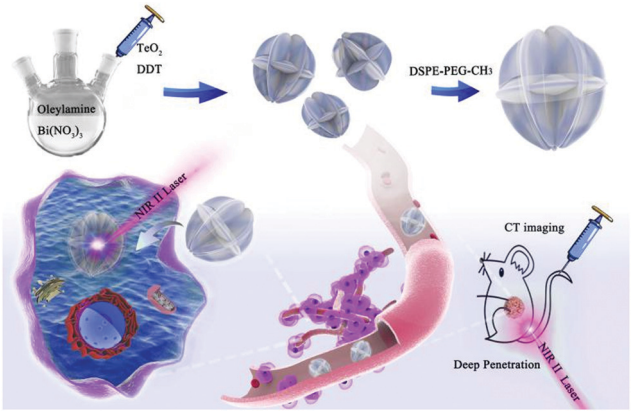

Scheme 1 Preparation of Bi_2Te_3@PEG superstructures for CT imaging-guided photothermal therapy in the second near-infrared biowindow.

have been exploited as CT contrast agents on account of the high atomic number and X-ray absorption coefficient of Bi, such as in Bi nanodots,[26] Bi-based chalcogenides,[27] BiOCl nanosheets[28] and so on. Additionally, these Bi-based nanomaterials have good absorption in the NIR-I region, indicating that Bi-based nanomaterials could serve as theranostic nanoagents for CT imaging and PTT.[29] However, as far as we know, there have been only a few reports on the development of Bi-based nanomaterials for PTT in the NIR-II biowindow.[30–32]

Bi_2Te_3 nanostructures, a kind of Bi-based chalcogenides, have exhibited potential in cancer theranostics, but only Bi_2Te_3 nanosheets prepared by chemical exfoliation have been investigated so far.[33] In this work, we synthesized carambola-like Bi_2Te_3 superstructures modified with PEGylated phospholipid (Bi_2Te_3@PEG) as a nanotheranostic agent for CT imaging-guided PTT in the NIR-II biowindow (Scheme 1). Benefiting from their carambola-like Bi_2Te_3 superstructure, Bi_2Te_3@PEG showed enhanced photoabsorption in the NIR-II region, resulting in a higher PCE (55.3% for 1064 nm) than that of Bi_2Te_3 nanoparticles. The tumors have been effectively eliminated after 14 d of treatment, demonstrating the good treatment effect of PTT in the NIR-II biowindow. Furthermore, Bi_2Te_3@PEG exhibited higher contrast densities as CT contrast agents than clinical iodine-based contrast agents owing to the high X-ray attenuation coefficient of Bi. These findings validate that Bi_2Te_3@PEG superstructures are a potential nanotheranostic agent for CT imaging-guided PTT in the NIR-II biowindow.

Experimental procedures

Materials

Tellurium dioxide (TeO_2), bismuth(III) nitrate [$Bi(NO_3)_3{\cdot}5H_2O$], bismuth(III) chloride ($BiCl_3$), tellurium (Te), oleylamine (OM), sodium hydroxide (NaOH), and dodecanethiol (DDT) were purchased from Aladdin-Reagent, Shanghai. 1,2-Diastearoyl-*sn-glycero*-3-phosphoethanolamine-*N*-[methoxy(polyethylene glycol)] (DSPE-PEG-CH_3) was purchased from TCI (Japan).

Preparation of Bi_2Te_3@PEG

Typically, $Bi(NO_3)_3{\cdot}5H_2O$ (0.3234 g) and OM (10 mL) were added to a flask and heated to 120 °C under N_2 protection to remove traces water. Afterward, the solution was heated up to 180 °C. At the same time, TeO_2 (0.1596 g) and DDT (2 mL) were heated to 110 °C for 15 minutes under N_2 protection in another flask. Then, the mixture was injected into the first solution quickly. Thereafter, the reaction was terminated using a water bath. Bi_2Te_3 was obtained by centrifugation and washed a few times with chloroform. Then, the obtained product was mixed with DSPE-PEG-CH_3 in chloroform and stirred overnight. Finally, the mixture was evaporated and washed a few times with deionized water.

Preparation of Bi_2Te_3 nanoparticles

First, CTAB (0.3 g) was dispersed in a mixture of ethanol and water. Then, 0.15 g of NaOH, 0.946 g of $BiCl_3$, and 574.2 g of Te were sequentially added into this mixture. After stirring for 15 minutes, 12 mmol $NaBH_4$ was introduced. Then, the mixture was poured into a 30 mL Teflon-lined autoclave and placed in a 210 °C oven for 24 h. Finally, Bi_2Te_3 nanoparticles were obtained by centrifugation and washed a few times with ethanol and deionized water.

Photothermal properties of Bi_2Te_3@PEG

Bi_2Te_3@PEG solutions (1 mL) with a variety of concentrations (0, 12.5, 25, 50, and 100 ppm) were exposed to a 1064 nm or 808 nm laser (1 W cm^{-2}) in the quartz cuvette for 10 min. Meanwhile, an infrared thermal imaging camera was employed to measure the temperature every 30 s and the thermal imaging images were taken every 2 min (FLIR T420, Fluke, USA). Thereafter, the temperature of the solution was cooled down naturally to investigate its PCE (η). The above experiments were repeated three times.

CT imaging properties

A CT scanner was employed to evaluate the CT imaging properties of Bi_2Te_3@PEG. Typically, different concentrations of iobitridol and Bi_2Te_3@PEG aqueous solutions (0, 0.25, 0.5, 1, and 2 mg mL^{-1}) of I and Bi were used to measure X-ray CT imaging *in vitro*. Then, Bi_2Te_3@PEG solution (2 mg mL^{-1}, 200 μL) was injected intravenously into tumor-bearing Kunming mice for CT imaging *in vivo*. And, CT images were recorded before and after the injection (3 and 24 h), respectively. Imaging parameters were given as follows: tube voltage, 120 kVp; tube current, 300 mA; thickness, 0.9 mm; field of view, 350 mm; and rotation time, 0.5 s.

Cytotoxicity and photothermal effects of Bi_2Te_3@PEG *in vitro*

Non-cancerous mouse fibroblast cells (L929) and human cervical cancer cells (HeLa) were inoculated into a 96-well plate. Then, Bi_2Te_3@PEG solutions with different concentrations (0, 12.5, 25, 50, and 100 ppm) were introduced in it and incubated for one day. Thereafter, the cell counting kit 8 (CCK-8) solution was diluted and added into the wells and a plate reader was employed to record the survival rate of the cells. To investigate the photothermal effects of Bi_2Te_3@PEG,

 This journal is © The Royal Society of Chemistry 2021

Published on 25 Mai 2021. Downloaded on 30/01/2026 18:03:13.

the Bi_2Te_3@PEG solutions with different concentrations (0, 12.5, 25, 50, and 100 ppm) were incubated with HeLa cells. After irradiation (1064 nm, 1 W cm^{-2}) for 10 min, the survival rate of the cells was detected by the CCK-8 solution and observed using an inverted fluorescence microscope.

Photothermal effects of Bi_2Te_3@PEG *in vivo*

40 female Kunming mice were selected for the *in vivo* therapy experiment. Typically, they were randomly divided into four groups after planted with U14 tumor cells, including (I) saline, (II) 1064 nm laser, (III) Bi_2Te_3@PEG (nanomaterials group), and (IV) Bi_2Te_3@PEG + 1064 nm (PTT group). Among them, groups III and IV were injected intravenously with Bi_2Te_3@PEG, while groups I and II were injected intravenously with saline every other day. At 24 h post injection, tumors in groups II and IV were exposed to a laser (1064 nm, 1 W cm^{-2}). During this time, the weight of the mice and tumor dimension were detected every other day. And, the tumor volume was calculated as follows: V = (tumor length) × (tumor width)^2/2. After the 2nd day of treatment, the tumor was dissected for pathological analysis. On the 15th day, the Kunming mice were sacrificed and the tumors were dissected to evaluate the therapeutic efficacy.

Long-term toxicology of Bi_2Te_3@PEG *in vivo*

Bi_2Te_3@PEG was injected intravenously into the Kunming mice. On the 15th day, a few of the mice were sacrificed, and their main organs were dissected and soaked in formalin solution for histopathological analysis. On the 30th day, the remaining mice were used for blood routine and blood biochemical analyses.

Results and discussion

Synthesis and characterization of Bi_2Te_3@PEG superstructures

Bi_2Te_3 was obtained by the high-temperature method according to a previous study.[34] As displayed in the scanning electron microscopy (SEM, Fig. 1A) and transmission electron microscope (TEM) images (Fig. 1B), the prepared Bi_2Te_3 show carambola-like superstructures with an average diameter of ~260 nm. Fig. 1C provides the lattice spacing of 0.322 nm, fitting with the (015) plane of Bi_2Te_3. The X-ray diffraction (XRD) pattern shown in Fig. S1 (ESI†) manifests that all characteristic diffractions match well with Bi_2Te_3 (JCPDS 72-2036). X-ray photoelectron spectroscopy (XPS) was used to determine the composition and surface valence states of Bi_2Te_3 (Fig. 1D). As shown in the high-resolution Bi 4f spectrum (Fig. 1E), the peaks of 162.4 and 157.1 eV are attributed to Bi $4f_{5/2}$ and Bi $4f_{7/2}$ of Bi_2Te_3, respectively, and the peaks at 158.6 and 163.9 eV can be assigned to the oxide surface of Bi_2Te_3. The Te 3d spectrum shown in Fig. 1F contains peaks at 582.2 and 572.0 eV, matching well with Te $3d_{3/2}$ and Te $3d_{5/2}$, respectively. In short, the valence of Bi_2Te_3 shown in XPS is in good compliance with the previous report.[35]

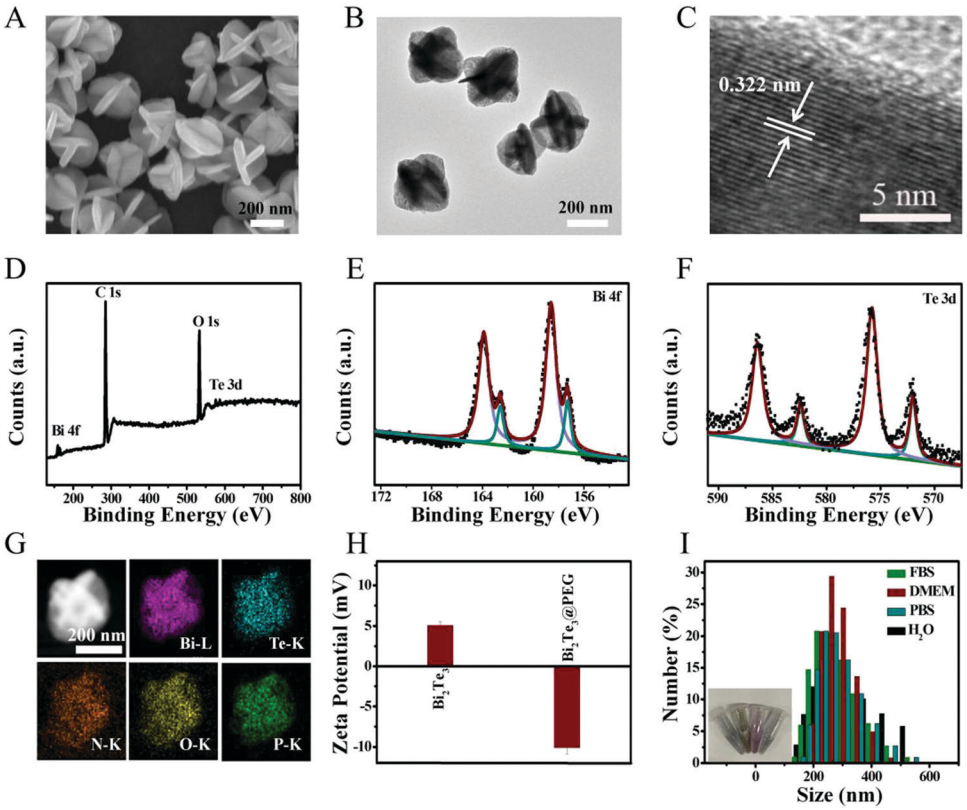

Fig. 1 (A) SEM image of Bi_2Te_3. (B) TEM image of Bi_2Te_3. (C) HRTEM image of Bi_2Te_3. (D) XPS spectra of Bi_2Te_3. (E) High-resolution Bi 4f spectrum of Bi_2Te_3. (F) High-resolution Te 3d spectrum of Bi_2Te_3. (G) STEM image and elemental mapping of Bi, Te, N, O, and P of Bi_2Te_3@PEG. (H) Zeta potential of Bi_2Te_3 and Bi_2Te_3@PEG. (I) Hydrodynamic size of Bi_2Te_3@PEG in H_2O, PBS, FBS, and DMEM.

Published on 25 Mai 2021. Downloaded on 30/01/2026 18:03:13.

Then, Bi_2Te_3 was modified with PEGylated phospholipid to improve the biocompatibility. As shown in Fig. S2 (ESI†), the morphology of Bi_2Te_3@PEG is unchanged after modification. Energy-dispersive X-ray (EDX) mapping shows that the Bi, Te, N, O, and P elements are distributed homogeneously in the Bi_2Te_3@PEG superstructures (Fig. 1G), indicating the successful coating of PEGylated phospholipid. As presented in Fig. S3 (ESI†), the characteristic IR bands at 2800–3000, 1715 and 1106 cm^{-1} assigned to $-CH_2$, O–P, and C–O–C appear in the Fourier transform infrared (FT-IR) spectrum of Bi_2Te_3@PEG. Moreover, the zeta potential analysis reveals that the potential value ranges from 5.07 mV to −10.11 mV after modification (Fig. 1H). These results further demonstrate the successful modification of PEGylated phospholipid. Furthermore, Bi_2Te_3@PEG superstructures exhibit good dispersibility in various solutions (Fig. 1I), including water, phosphate-buffered saline (PBS), fetal bovine serum (FBS), and Dulbecco's modified Eagle's medium (DMEM), offering them great potential for bioapplications.

Photothermal properties of Bi_2Te_3@PEG superstructures

Benefiting from the unique carambola-like superstructure, Bi_2Te_3@PEG superstructures have stronger absorption from the UV to the NIR-II region compared with that of Bi_2Te_3 nanoparticles prepared following previous reports (Fig. 2A).[36] The carambola-like superstructure make the Bi_2Te_3@PEG superstructures act as good laser cavity mirrors, which could enhance the capacity of photoabsorption and reflection of the laser (Fig. 2B).[37] To further demonstrate the effect of the superstructures on the photothermal properties, we compared the temperature changes of Bi_2Te_3@PEG superstructure and Bi_2Te_3 nanoparticle solutions under irradiation (1064 nm, 1 W cm^{-2}). Fig. 2C–E and Fig. S4 and S5 (ESI†) indicated that the temperature changes were dependent on both the concentration of the solution and the power density of the 1064 nm laser. In comparison with deionized water, the temperature of Bi_2Te_3@PEG solution (100 ppm) increased to 48.1 °C within 10 min under irradiation, indicating the excellent photothermal performance of Bi_2Te_3@PEG. By contrast, the temperature elevation of Bi_2Te_3 nanoparticles merely reached to 37.8 °C under the same conditions. The PCE (η) of Bi_2Te_3@PEG was calculated as 55.3% according to the fitted cooling curve (Fig. 2F), which was much higher than that of the Bi_2Te_3 nanoparticles (40.88% according to Fig. 2G). And, the good photothermal performance of Bi_2Te_3@PEG was also obtained by employing an 808 nm laser (1 W cm^{-2}, Fig. S6, ESI†), further demonstrating the effectiveness of the superstructures for improving the photoabsorption. Furthermore, the photothermal performance of Bi_2Te_3@PEG exhibited no significant difference after a five-cycle process, suggesting their good photothermal

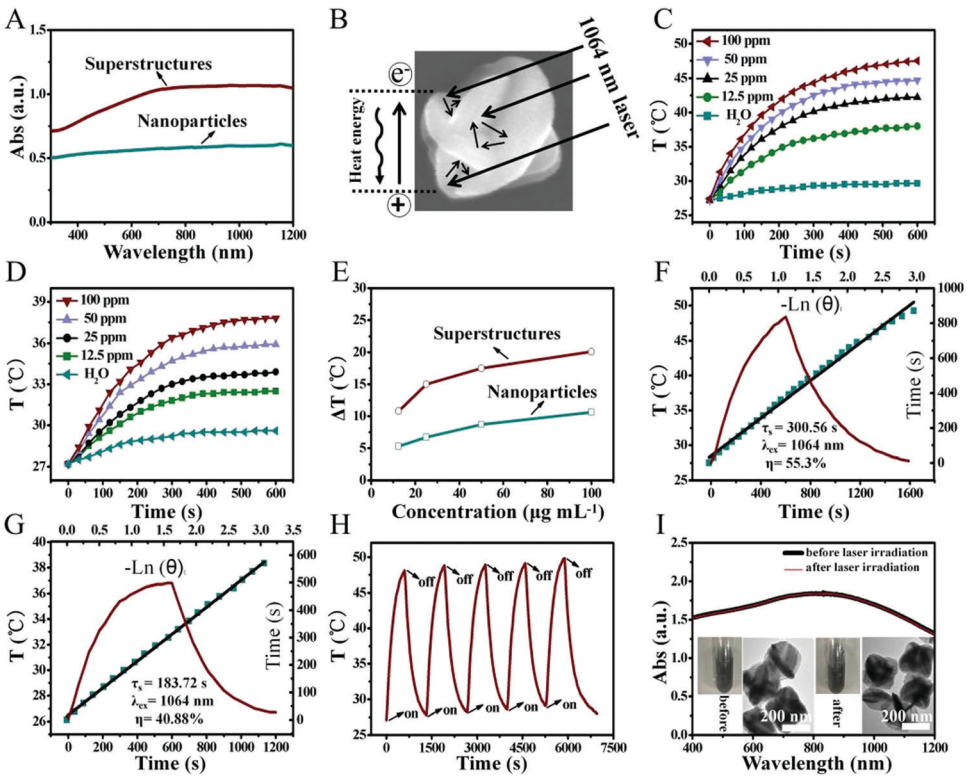

Fig. 2 (A) UV–vis spectra of Bi_2Te_3@PEG and Bi_2Te_3 nanoparticles. (B) Schematic representation of a carambola-like Bi_2Te_3@PEG superstructure acting as good laser cavity mirrors. Temperature curves of (C) Bi_2Te_3@PEG and (D) Bi_2Te_3 nanoparticles at various concentrations (0, 12.5, 25, 50, and 100 ppm) under irradiation (1064 nm, 1 W cm^{-2}). (E) The ΔT of Bi_2Te_3@PEG and Bi_2Te_3 nanoparticles. Heating and cooling curves of (F) Bi_2Te_3@PEG and (G) Bi_2Te_3 nanoparticles, with a fitted line acquired from the cooling section. (H) Temperature of Bi_2Te_3@PEG over five on/off cycles of the 1064 nm laser. (I) UV–vis spectrum of Bi_2Te_3@PEG before and after irradiation with the 1064 nm laser.

 This journal is © The Royal Society of Chemistry 2021

Published on 25 Mai 2021. Downloaded on 30/01/2026 18:03:13.

stability (Fig. 2H). This result was further confirmed by their unchanged UV/Vis spectrum and morphology after irradiation with the 1064 nm laser (Fig. 2I). All these results validate that Bi_2Te_3@PEG superstructures are potential PTAs for PTT in the NIR-II biowindow.

CT imaging of Bi_2Te_3@PEG *in vitro* and *in vivo*

Because of the good X-ray attenuation capacity of Bi, we further evaluated the availability of Bi_2Te_3@PEG to act as a CT contrast agent. Compared with iobitridol (a commercial CT contrast agent), Bi_2Te_3@PEG showed enhanced contrast signals at equivalent concentrations (Fig. 3A and B), which should be attributed to the high K-edge value of Bi. Inspired by the above results, we further investigated their imaging capacity *in vivo* using the U14 tumor-bearing mice model. After intravenous injection of Bi_2Te_3@PEG (2 mg mL^{-1}, 200 μL), CT signals of the tumor were detected using a CT scanner. As depicted in Fig. 3C, the tumor area became significantly brighter 24 h after the injection, reflecting the good accumulation ability of Bi_2Te_3@PEG in the tumor area. All these findings suggest that Bi_2Te_3@PEG could act as a promising CT contrast agent for cancer diagnosis.

Cytotoxicity and anticancer effects of Bi_2Te_3@PEG *in vitro*

Motivated by the excellent photothermal performance of Bi_2Te_3@PEG, we further investigated its potential as a PTA for PTT. First, the cytotoxicity was assessed by incubating different concentrations of Bi_2Te_3@PEG (0, 12.5, 25, 50, and 100 ppm) with L929 or HeLa cells for 24 h. Fig. 4A revealed that the survival rates were still higher than 90% for both L929 and HeLa cells even at the concentration of 100 ppm, demonstrating the good biocompatibility of Bi_2Te_3@PEG. Furthermore, we assessed the anticancer effect of Bi_2Te_3@PEG by the CCK-8 assay. The survival rates of L929 and HeLa cells showed a sharp decline with the increasing of Bi_2Te_3@PEG concentration after irradiation (1064 nm, 1 W cm^{-2}) for 10 minutes (Fig. 4B), indicating that hyperthermia produced by Bi_2Te_3@PEG could effectively kill the cancer cells in a few minutes. The results of calcein AM and propidium iodide (PI) staining further demonstrated the good anticancer performance of Bi_2Te_3@PEG.

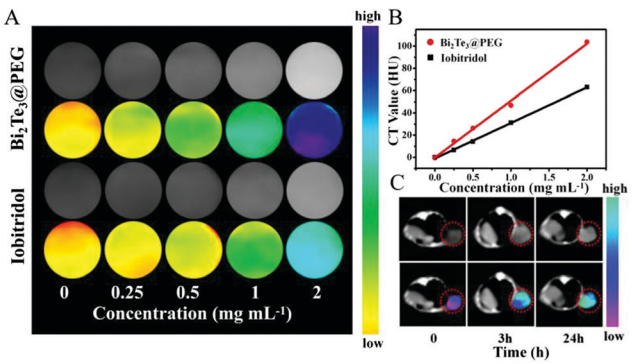

Fig. 3 (A) CT images and (B) CT values (HU) of Bi_2Te_3@PEG and iobitridol at various concentrations of Bi and I *in vitro*. (C) CT images of Kunming mice bearing a tumor at 0, 3, and 24 h after injection of the Bi_2Te_3@PEG.

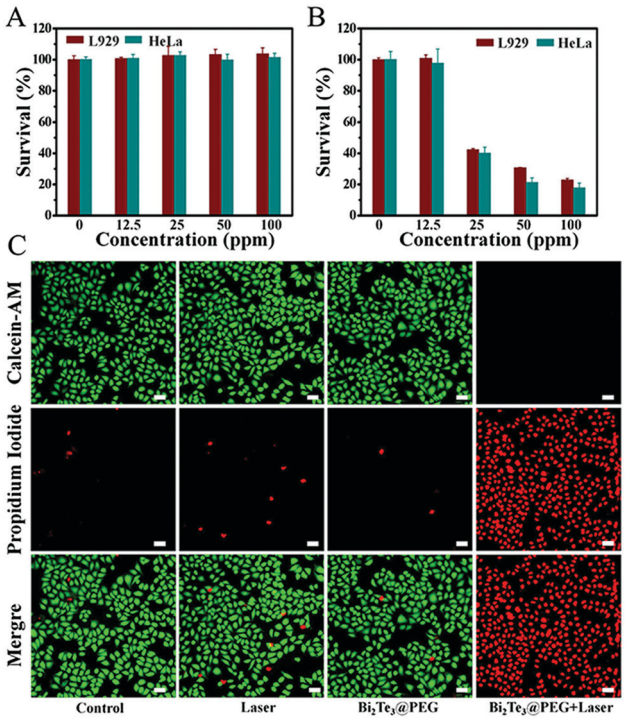

Fig. 4 (A) The survival rates of L929 and HeLa cells treated with a variety of concentrations of Bi_2Te_3@PEG (0, 12.5, 25, 50, and 100 ppm). (B) L929 and HeLa cell viabilities with the treatment of Bi_2Te_3@PEG + 1064 nm laser (1 W cm^{-2}). (C) Fluorescence images of HeLa cells in different groups (scale bars: 50 μm).

As displayed in Fig. 4C and Fig. S7 (ESI†), similar to that in the control and laser groups, both HeLa and L929 cells in the Bi_2Te_3@PEG (100 ppm) group showed strong green fluorescence, which should be attributed to their good biocompatibility. By contrast, cells in the Bi_2Te_3@PEG (100 ppm) + 1064 nm (1 W cm^{-2}, 10 min) group, as expected, revealed strong red fluorescence and negligible green fluorescence, further demonstrating the remarkable PTT treatment effect *in vitro*.

Anticancer effects of Bi_2Te_3@PEG *in vivo*

Inspired by the good anticancer performance of Bi_2Te_3@PEG *in vitro*, we further evaluated the treatment effects of Bi_2Te_3@PEG *in vivo* using the U14 tumor-bearing Kunming mice model. The photothermal performance of Bi_2Te_3@PEG *in vivo* was investigated by infrared thermal imaging. Mice bearing tumor were exposed to the laser (1064 nm, 1.0 W cm^{-2}) at 24 h post injection of Bi_2Te_3@PEG, and the variation of the temperature in the tumor area was measured using an infrared thermal imaging camera. As depicted in Fig. S8 (ESI†), the temperature of the tumor rapidly increased to 57 °C within 10 min, whereas no significant heating was observed in the laser group, demonstrating that the remarkable photothermal effects of Bi_2Te_3@PEG offer them great feasibility for local heating of the tumor. Then, the mice were randomly allocated into the following groups: (I) control group, (II) 1064 nm laser group, (III) Bi_2Te_3@PEG group, and (VI) Bi_2Te_3@PEG + laser (1064 nm, 1 W cm^{-2}) group. The size of the tumor and the weight of the

Published on 25 Mai 2021. Downloaded on 30/01/2026 18:03:13.

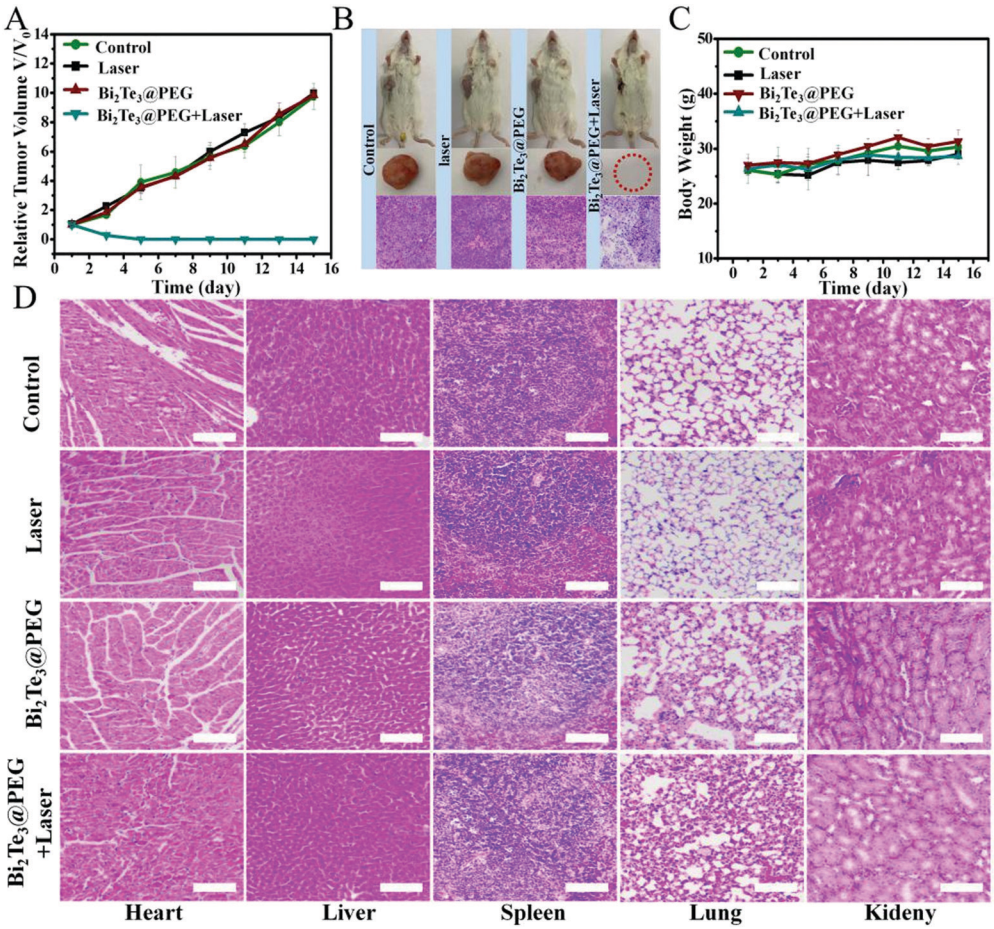

Fig. 5 (A) Volume of tumor in different groups. (B) Pictures of mice, corresponding appearance and H&E staining of tumor tissues after various treatments. (C) Weight of mice in the four groups. (D) H&E staining photographs of essential organs (scale bars: 100 μm).

mice were measured every other day. In contrast with groups I, II, and III, the tumors in treatment group VI were completely eradicated after twice treatments, and no recurrence was observed within 14 days (Fig. 5A), implying the remarkable PTT efficacy of Bi_2Te_3@PEG in the NIR-II biowindow. In addition, the histological assay (haematoxylin–eosin staining (H&E staining)) showed that the tumor tissues suffered severe damage in treatment group VI, whereas no significant necrosis was observed in the other groups, further demonstrating the good treatment effect of Bi_2Te_3@PEG (Fig. 5B). Furthermore, there is a negligible difference in weight of the mice in all groups within 14 days, implying the low acute toxicity of Bi_2Te_3@PEG (Fig. 5C). All these results confirmed that Bi_2Te_3@PEG can serve as a promising PTA for highly effective photothermal therapy in the NIR-II biowindow.

In vivo toxicology of Bi_2Te_3@PEG

The biosafety of nanomaterials is a crucial factor for further biomedical applications. First, the histological assay of the essential organs of mice was investigated after intravenous injection with Bi_2Te_3@PEG for 15 days. Fig. 5D revealed that no obvious damage could be viewed in all groups, indicating that Bi_2Te_3@PEG exhibited low side effects on the major organs *in vivo* applications. Furthermore, blood routine and blood biochemical analyses were carried out at 30 d post injection of Bi_2Te_3@PEG. Fig. S9 (ESI†) shows that there was no obvious discrepancy of the blood index between the control and Bi_2Te_3@PEG groups, further demonstrating the negligible long-term toxicity of Bi_2Te_3@PEG.

Conclusions

In summary, carambola-like Bi_2Te_3@PEG superstructures have been successfully synthesized and served as novel nanotheranostic agents for CT imaging-guided PTT in the NIR-II biowindow. Compared with Bi_2Te_3 nanoparticles, Bi_2Te_3@PEG exhibited higher optical absorption in the NIR-II biowindow and higher PCE (55.3% for 1064 nm), which could be attributed to their carambola-like superstructures that can act as good laser cavity mirrors. Besides, because of the good X-ray attenuation capacity of Bi, Bi_2Te_3@PEG could serve as a good contrast agent for CT imaging *in vitro* and *in vivo*. Importantly, Bi_2Te_3@PEG could eradicate tumors with the irradiation at 1064 nm using a safe power density of 1 W cm^{-2}, achieving highly effective cancer therapy. This work will provide new insights for designing highly effective PTAs with good photothermal performances through the regulation of the structure.

 This journal is © The Royal Society of Chemistry 2021

Conflicts of interest

There are no conflicts to declare.

Acknowledgements

This work was supported by the financial aid from the National Natural Science Foundation of China (Grants 52022094, 22020102003, 21521092, 21590794, 51502284, 5207214 and 21673220), the Strategic Priority Research Program of the Chinese Academy of Sciences (Grant XDB20030300), and the Youth Innovation Promotion Association of Chinese Academy of Sciences (Grant 2019232).

Notes and references

Published on 25 Mai 2021. Downloaded on 30/01/2026 18:03:13.

1 D. Wu, X. Duan, Q. Guan, J. Liu, X. Yang, F. Zhang, P. Huang, J. Shen, X. Shuai and Z. Cao, *Adv. Funct. Mater.*, 2019, **29**, 1900095.
2 P. Jia, H. Ji, S. Liu, R. Zhang, F. He, L. Zhong and P. Yang, *J. Mater. Chem. B*, 2021, **9**, 101–111.
3 M. Ha, S. H. Nam, K. Sim, S. E. Chong, J. Kim, Y. Kim, Y. Lee and J. M. Nam, *Nano Lett.*, 2021, **21**, 731–739.
4 F. Xu, X. Li, H. Chen, M. Jian, Y. Sun, G. Liu, L. Ma and Z. Wang, *J. Mater. Chem. B*, 2020, **8**, 10136–10145.
5 Q. Wang, H. Wang, Y. Yang, L. Jin, Y. Liu, Y. Wang, X. Yan, J. Xu, R. Gao, P. Lei, J. Zhu, Y. Wang, S. Song and H. Zhang, *Adv. Mater.*, 2019, **31**, 1904836.
6 X. Chen, X. Zhu, T. Xu, M. Xu, Y. Wen, Y. Liu, J. Liu and X. Qin, *J. Mater. Chem. B*, 2019, **7**, 112–122.
7 C. Zhan, Y. Huang, G. Lin, S. Huang, F. Zeng and S. Wu, *Small*, 2019, **15**, 1900309.
8 F. Zhou, M. Wang, T. Luo, J. Qu and W. R. Chen, *Biomaterials*, 2021, **265**, 120421.
9 D. Wang, N. Zhang, X. Jing, Y. Zhang, Y. Xu and L. Meng, *J. Mater. Chem. B*, 2020, **8**, 8271–8281.
10 Y. Qiu, D. Ding, W. Sun, Y. Feng, D. Huang, S. Li, S. Meng, Q. Zhao, L. J. Xue and H. Chen, *Nanoscale*, 2019, **11**, 16351–16361.
11 L. Dong, K. Li, D. Wen, Y. Lu, K. Du, M. Zhang, X. Gao, J. Feng and H. Zhang, *Nanoscale*, 2019, **11**, 12853–12857.
12 Z. Zhou, B. Li, C. Shen, D. Wu, H. Fan, J. Zhao, H. Li, Z. Zeng, Z. Luo, L. Ma and C. Tan, *Small*, 2020, **16**, 2004173.
13 Y. Liu, W. Zhen, Y. Wang, J. Liu, L. Jin, T. Zhang, S. Zhang, Y. Zhao, S. Song, C. Li, J. Zhu, Y. Yang and H. Zhang, *Angew. Chem., Int. Ed.*, 2019, **58**, 2407–2412.
14 Y. Liu, W. Zhen, Y. Wang, J. Liu, L. Jin, T. Zhang, S. Zhang, Y. Zhao, N. Yin, R. Niu, S. Song, L. Zhang and H. Zhang, *Nano Lett.*, 2019, **19**, 5093–5101.
15 J. Zeng, M. Wu, S. Lan, J. Li, X. Zhang, J. Liu, X. Liu, Z. Wei and Y. Zeng, *J. Mater. Chem. B*, 2018, **6**, 7889–7897.
16 Y. Chen, B. Sun, X. Jiang, Z. Yuan, S. Chen, P. Sun, Q. Fan and W. Huang, *J. Mater. Chem. B*, 2021, **9**, 1002–1008.
17 W. Zhen, S. An, W. Wang, Y. Liu, X. Jia, C. Wang, M. Zhang and X. Jiang, *Nanoscale*, 2019, **11**, 9906–9911.
18 S. Zhang, L. Jin, J. Liu, Y. Liu, T. Zhang, Y. Zhao, N. Yin, R. Niu, X. Li, D. Xue, S. Song, Y. Wang and H. Zhang, *Nano-Micro Lett.*, 2020, **12**, 180.
19 Y. Liu, J. Wu, Y. Jin, W. Zhen, Y. Wang, J. Liu, L. Jin, S. Zhang, Y. Zhao, S. Song, Y. Yang and H. Zhang, *Adv. Funct. Mater.*, 2019, **29**, 1904678.
20 W. Hu, X. Miao, H. Tao, A. Baev, C. Ren, Q. Fan, T. He, W. Huang and P. N. Prasad, *ACS Nano*, 2019, **13**, 12006–12014.
21 W. Liao, P. Lei, J. Pan, C. Zhang, X. Sun, X. Zhang, C. Yu and S. K. Sun, *Biomaterials*, 2019, **203**, 1–11.
22 Y. Fan, W. Tu, M. Shen, X. Chen, Y. Ning, J. Li, T. Chen, H. Wang, F. Yin, Y. Liu and X. Shi, *Adv. Funct. Mater.*, 2020, **30**, 1909285.
23 J. Xu, P. Yang, M. Sun, H. Bi, B. Liu, D. Yang, S. Gai, F. He and J. Lin, *ACS Nano*, 2017, **11**, 4133–4144.
24 F. Li, T. Li, D. Zhi, P. Xu, W. Wang, Y. Hu, Y. Zhang, S. Wang, J. M. Thomas, J. B. Norman, W. Ding, L. Yan and B. Qiu, *Biomaterials*, 2020, **256**, 120219.
25 R. Luo, L. Chen, Q. Li, J. Zhou, L. Mei, Z. Ning, Y. Zhao, M. Liu, X. Lai, J. Bi, W. Yin and D. Gao, *Inorg. Chem.*, 2020, **59**, 17906–17915.
26 P. Lei, R. An, P. Zhang, S. Yao, S. Song, L. Dong, X. Xu, K. Du, J. Feng and H. Zhang, *Adv. Funct. Mater.*, 2017, **27**, 1702018.
27 Y. Cheng, Y. Chang, Y. Feng, H. Jian, X. Wu, R. Zheng, K. Xu and H. Zhang, *Adv. Mater.*, 2019, **31**, 1806808.
28 C. Dai, R. Hu, C. Wang, Z. Liu, S. Zhang, L. Yu, Y. Chen and B. Zhang, *Nanoscale Horiz.*, 2020, **5**, 857–868.
29 P. Lei, R. An, X. Zheng, P. Zhang, K. Du, M. Zhang, L. Dong, X. Gao, J. Feng and H. Zhang, *Nanoscale*, 2018, **10**, 16765–16774.
30 S. Dong, Y. Dong, T. Jia, S. Liu, J. Liu, D. Yang, F. He, S. Gai, P. Yang and J. Lin, *Adv. Mater.*, 2020, **32**, 2002439.
31 J. Li, D. Zhu, W. Ma, Y. Yang, G. Wang, X. Wu, K. Wang, Y. Chen, F. Wang, W. Liu and Y. Yuan, *Nanoscale*, 2020, **12**, 17064–17073.
32 A. Li, X. Li, X. Yu, W. Li, R. Zhao, X. An, D. Cui, X. Chen and W. Li, *Biomaterials*, 2017, **112**, 164–175.
33 J. Bai, X. Jia, Y. Ruan, C. Wang and X. Jiang, *Inorg. Chem.*, 2018, **57**, 10180–10188.
34 D. Yao, W. Xin, Z. Liu, Z. Wang, J. Feng, C. Dong, Y. Liu, B. Yang and H. Zhang, *ACS Appl. Mater. Interfaces*, 2017, **9**, 9840–9848.
35 Q. Wang, K. Cui, J. Li, Y. Wu, Y. Yang, X. Zhou, G. Ma, Z. Yang, Z. Lei and S. Ren, *Nanoscale*, 2020, **12**, 16208–16214.
36 Z. Zhou, W. Zhang, L. Zhang, Y. Cao, Z. Xu, Y. Kang and P. Xue, *Biomater. Sci.*, 2020, **8**, 5874–5887.
37 Q. Tian, M. Tang, Y. Sun, R. Zou, Z. Chen, M. Zhu, S. Yang, J. Wang, J. Wang and J. Hu, *Adv. Mater.*, 2011, **23**, 3542–3547.